

The ALPINE-ALMA [C II] Survey: [C II] 158 micron Emission Line Luminosity Functions at $z \sim 4 - 6$

Lin Yan¹, A. Sajina², F. Loiacono^{3,4}, G. Lagache⁵, M. Béthermin⁵, A. Faisst⁶, M. Ginolfi⁷,
O. Le Fèvre⁸, C. Gruppioni⁴, P. L. Capak⁶, P. Cassata⁹, D. Schaerer^{7,10}, J. D. Silverman^{11,12},
S. Bardelli⁴, M. Dessauges-Zavadsky⁷, A. Cimatti^{3,4}, N. P. Hathi¹³, B. C. Lemaux¹⁴, E. Ibar¹⁵,
G. C. Jones^{16,17}, Anton M. Koekemoer¹³, P. A. Oesch^{7,18}, M. Talia^{3,4}, F. Pozzi^{3,4}, D. A. Riechers¹⁹,
L. A. M. Tasca⁸, Sune Toft^{18,20}, L. Vallini²¹, D. Vergani⁴, G. Zamorani⁴ and E. Zucca⁴

¹*The Caltech Optical Observatories, California Institute of Technology, Pasadena, CA 91125, USA*

²*Department of Physics and Astronomy, Tufts University, Medford, MA 02155, USA*

³*Dipartimento di Fisica e Astronomia, Università di Bologna via Gobetti 93/2, I-40129 Bologna, Italy*

⁴*Osservatorio di Astrofisica e Scienza dello Spazio di Bologna via Gobetti 93/3, I-40129 Bologna, Italy*

⁵*Aix Marseille Université, CNRS, CNES, LAM, Marseille, France*

⁶*Infrared Processing and Analysis Center, California Institute of Technology, Pasadena, CA 91125, USA*

⁷*Observatoire de Genève, Université de Genève 51 Ch. des Maillettes, 1290 Versoix, Switzerland*

⁸*Aix Marseille Université, CNRS, CNES, LAM (Laboratoire d'Astrophysique de Marseille), 13013, Marseille, France*

⁹*Dipartimento di Fisica e Astronomia, Università di Padova, Vicolo dell'Osservatorio, 3 35122 Padova, Italy*

¹⁰*Institut de Recherche en Astrophysique et Planétologie - IRAP, CNRS, Université de Toulouse, UPS-OMP, 14, avenue E. Belin, F31400 Toulouse, France*

¹¹*Kavli Institute for the Physics and Mathematics of the Universe, The University of Tokyo, Kashiwa, Japan
277-8583 (Kavli IPMU, WPI)*

¹²*Department of Astronomy, School of Science, The University of Tokyo, 7-3-1 Hongo, Bunkyo, Tokyo 113-0033,
Japan*

¹³*Space Telescope Science Institute, 3700 San Martin Dr., Baltimore, MD 21218, USA*

¹⁴*Department of Physics, University of California, Davis, One Shields Ave., Davis, CA 95616, USA*

¹⁵*Instituto de Física y Astronomía, Universidad de Valparaíso, Avda. Gran Bretaña 1111, Valparaíso, Chile*

¹⁶*Cavendish Laboratory, University of Cambridge, 19 J. J. Thomson Ave., Cambridge CB3 0HE, UK*

¹⁷*Kavli Institute for Cosmology, University of Cambridge, Madingley Road, Cambridge CB3 0HA, UK*

¹⁸*Cosmic Dawn Center (DAWN)*

¹⁹*Cornell University, Space Sciences Building, Ithaca, NY 14853, USA*

²⁰*Niels Bohr Institute, University of Copenhagen, Lyngbyvej 2, DK-2100 Copenhagen, Denmark*

²¹*Leiden Observatory, Leiden University, PO Box 9500, NL-2300 RA Leiden, the Netherlands*

Submitted to ApJ

Abstract

We present the [C II] 158 μ m line luminosity functions (LFs) at $z \sim 4 - 6$ using the ALMA observations of 118 sources, which are selected to have UV luminosity $M_{1500\text{\AA}} <$

–20.2 and optical spectroscopic redshifts in COSMOS and ECDF-S. Of the 118 targets, 75 have significant [CII] detections and 43 are upper limits. With this UV-selected sample, we set stringent lower bounds to the volume density of [CII] emitters at $z \sim 4 - 6$. Our derived LFs are consistent with the $z \sim 0$ [CII] LF at $\lesssim 10^9 L_\odot$, but show a hint of an excess of [CII] emitters at the luminous end ($> 10^9 L_\odot$) compared to $z \sim 0$. This excess is consistent with a potential population of [CII]-bright UV-faint sources that are largely excluded from the ALPINE target selection. To further constrain such sources, in a companion analysis, Loiacono et al. (2020) estimate the [CII] LF based on serendipitous [CII] sources in the ALPINE maps. Their resulting single data point is consistent with the excess we observe at the high luminosity end. Combined, these studies suggest possible redshift evolution in the [CII] LFs at high luminosity between $z \sim 5$ and 0. This conclusion is further supported by the inferred [CII] LFs from the far-IR and CO LFs at $z \sim 4 - 6$. Integrating our estimate on the best-fit [CII] LF, we set a constraint on molecular gas mass density at $z \sim 4 - 6$, with $\rho_{mol} \sim (2 - 7) \times 10^7 M_\odot \text{Mpc}^{-3}$. This is broadly consistent with previous studies, although the uncertainties span more than an order of magnitude. Finally, we find that available model predictions tend to underestimate the number densities of [CII] emitters at $z \sim 5$.

Keywords: galaxies: high-redshift galaxies:ISM - galaxies: luminosity function

1. Introduction

Galaxies in the distant Universe are thought to be more gas rich than low redshift systems. CO observations using Plateau de Bure Interferometer (PdBI) and NOthern Extended Millimeter Array (NOEMA) have provided quantitative measurements of gas fractions at $z \sim 1 - 2$ (Freundlich et al. 2019). However, at high redshifts, studies of gas content of galaxies have not been possible for large number of sources until the advent of the Atacama Large Millimeter/submillimeter Array (ALMA). This amazing facility has opened up new vistas for astronomical research, particularly for the high redshift Universe. In particular, it allows us to probe the InterStellar Medium (ISM) of galaxies in the early Universe, through far-infrared fine structure lines. It is now possible to measure both dust content using far-infrared/submillimeter continuum emission as well as ionized and molecular gas using far-infrared fine structure lines from galaxies in the early Universe.

The [CII] 158 μm emission is the strongest far-infrared fine-structure line. It can reach as high as a few percent of the galaxy total infrared luminosity. The [CII] line arises from collisionally excited C^+ ions. The ionization potential of C^+ is quite shallow, only 11.26 eV, and the critical electron number density is also small, $\sim 3 \times 10^3 \text{cm}^{-3}$ at $T = 100 \text{K}$ (Goldsmith et al. 2012). Both of these factors make the [CII] line the most efficient and dominant coolant for a variety of ISM, including neutral and ionized diffuse ISM.

Because of its high luminosity, the [CII] 158 μm line is considered the best probe of gas content in galaxies at redshift > 4 when this transition moves into the ALMA band 7. Since ALMA operations began in 2011, many individual detections of [CII] 158 μm lines at $z > 4$ have been published for a variety of objects, including normal star forming galaxies, QSOs and Ultraluminous infrared galaxies (ULIRG) (e.g. Wang et al. 2013; Riechers et al. 2014; Willott et al. 2015; Capak et al. 2015; Emonts et al. 2015;

Barro et al. 2017; Fudamoto et al. 2017; Zanella et al. 2018). In particular, the superb spatial resolution from ALMA has revealed many stunning discoveries of large, extended gas reservoir, gaseous companions and the associated kinematics (Jones et al. 2017; Shao et al. 2017; Lelli et al. 2018).

Today, the ever increasing number of [C II] 158 μm detections at high redshift from ALMA has naturally led to several questions regarding their population statistics. What is the volume density of [C II] emitters at $z \sim 4 - 6$? What is the [C II] line luminosity function (LF) at $z \sim 4 - 6$? Does it evolve strongly with redshift in comparison with that of low- z ? The recently published [C II] LF at $z \sim 0$ (Hemmati et al. 2017) serves as the useful local bench-mark when we discuss the redshift evolution.

In recent years, quite a few theoretical studies were published to model the observed CO and [C II] emission at high redshifts (Popping et al. 2016; Vallini et al. 2015; Katz et al. 2017; Olsen et al. 2017; Carniani et al. 2018; Lagache et al. 2018; Pallottini et al. 2019; Ferrara et al. 2019). Most of these cosmological simulations including radiative transfer are focused on understanding the correlation and deviations around the [C II] luminosity and star formation rate relation. Although some of these models can reproduce $z \sim 4 - 5$ luminous [C II] emitters found by the ALMA observations of Capak et al. (2015) and Willott et al. (2015), only two studies made predictions on [C II] LFs (Popping et al. 2016; Lagache et al. 2018). However, our measurements of [C II] LF at $z \sim 0$ (Hemmati et al. 2017) has already ruled out the Popping et al. (2016) model. Because [C II] emission involves many complex processes (Ferrara et al. 2019), it is now becoming urgent to properly measure the [C II] line LF at $z \sim 4 - 6$ and provide constraints to theoretical models.

The goal of this paper is to address these questions, using a unique set of observations taken

by the ALMA Large Program to INvestigate CII at Early times (ALPINE) survey (Le Fèvre et al. 2019; Faisst et al. 2020; Bethermin et al. 2020).

Our paper is organized as follows. §2 describes the ALPINE survey, the observations and the associated [C II] 158 μm line measurements. §3.1 discusses the methodology. The main results and conclusions are presented in §4 and §5.

Throughout the paper, all magnitudes are in AB system and the adopted cosmological parameters are $\Omega_{\Lambda,0} = 0.7$, $\Omega_{M,0} = 0.3$, $H_0 = 70 \text{ km s}^{-1} \text{ Mpc}^{-1}$.

2. Data

2.1. Summary of the ALPINE survey

The [C II] emission line fluxes are measured from the ALMA data taken by ALPINE. A detailed description of this survey is discussed in Le Fèvre et al. (2019). The reduction of ALPINE data and the association with the extensive multi-wavelength ancillary data are presented in Bethermin et al. (2020) and Faisst et al. (2019), respectively. A summary of the salient points of this survey is following.

ALPINE is a targeted survey, obtaining the [C II] spectral line and continuum observations with ALMA band 7 (275 - 373 GHz) for 118 main sequence galaxies, selected by their UV luminosity at 1500 Å (Note: not by stellar mass). These 118 galaxies are chosen to have optical spectroscopic redshifts in two intervals, $z \sim 4.40 - 4.58$ and $z \sim 5.14 - 5.85$ and to have 1500 Å absolute magnitude $M_{1500\text{Å}} \leq -20.2 \text{ mag}$. These targets have stellar masses of $10^{8.5} - 10^{11} M_{\odot}$ with an average value of $10^{9.7} M_{\odot}$ (Faisst et al. 2019). The redshift slice of 4.6 - 5.12 was excluded because the redshifted [C II] lines would fall in a low transmission window for ALMA. It is worth noting that the ALPINE targets have $M_{1500\text{Å}} < -20.2$ (*i.e.* $L_{1500\text{Å}} > 0.6L^*$), 0.76 magnitude lower luminos-

ity than the $M_{1500\text{\AA}}^* = -20.96$ for the UV LF at $z \simeq 4.5 - 5.5$ (Ono et al. 2018).

2.2. The [CII] emission line measurements

As discussed in Béthermin et al. (2020), the mean [CII] line flux root mean square (RMS) is 0.14 Jy km/s for this sample. The spectral maps have yielded 75 [CII] emission lines with the peak flux to noise ratio $\text{SNR}_{\text{peak}} \geq 3.5\sigma$ and 43 non-detections ($< 3.5\sigma$). In contrast to the high fraction of [CII] detections, the continuum maps have found only 23 detections at $\geq 3\sigma$. The high fraction of [CII] detection supports the correlation between the integrated [CII] luminosity and star formation rate (SFR). Schaerer et al. (2020) investigates this topic using the ALPINE data.

Another significant result is that a good fraction of the $z \sim 4 - 6$ sources is resolved – both spatially and kinematically – and many of them have multiple components and are clearly interacting. Several ALPINE papers (Le Fèvre et al. 2019; Béthermin et al. 2020; Loiacono et al. 2020) discuss this property. Jones et al. (2019) has focused on one triple merger system, deimos_cosmos_818760, with three [CII] components. Therefore, measuring the total line flux correctly is important for our calculations.

Since a large fraction of our sources are marginally resolved, their total line fluxes are generally larger than their peak fluxes, which are good representations of the total line fluxes only for point sources. Béthermin et al. (2020) has designed three different methods to measure total line fluxes. One is a simple circular aperture photometry within a $1.5''$ radius (f_{aper}). The second method is to sum up all fluxes within a 2σ contour above the background in the zero-moment map (f_{clipped}). And the last is a 2-dimensional elliptical Gaussian fitting method (f_{fit}). Overall, these three methods give good agreement. For example, the 2D-fit and 2σ -clipped fluxes are consistent, with a small offset of 3% and standard deviation of

only 0.17. As expected, aperture fluxes suffer larger errors, especially for faint sources (see Figure 15 in Béthermin et al. (2020)). The aperture fluxes tend to under-estimate the total fluxes compared with that of f_{fit} . For example, the mean and median of $f_{\text{aper}}/f_{\text{fit}}$ are 0.85 and 0.93 respectively. For this paper, we computed the LFs using f_{fit} and f_{clipped} . As shown in Figure 5, the differences are within the errors, see details in §4.

One important and complex question is how to deal with [CII] sources with multiple components. This paper adopts the total [CII] flux measurements for all of the sources provided by Béthermin et al. (2020), without deblending (see gold and red contours in Figure C.4 - 6 in that paper). The rationale is that the sample has only four systems with multiple components at comparable brightness (within a factor of a few). For four of these (vuds_cosmos_5100822662, deimos_cosmos_818760, deimos_cosmos_873321, deimos_cosmos_434239), each has two components separated by $\leq 1''$ and with velocity differences $\leq 200 - 300$ km/s (see Figure C.1 - 6 of Béthermin et al. 2020). Our paper considers these two components are physically connected and belong to one system. Worth noting that deimos_cosmos_818760 is in fact a triple system, with a third, fainter component $\geq 2''$ away. Our calculation does not include the fluxes from this third system (see Jones et al. (2019)). Finally, we comment on vuds_cosmos_5101209780, whose primary target (component a) has a companion (b) at a separation of $> 2''$ with a flux brighter by a factor of 2. Our paper only considers Component a . Loiacono et al. (2020) regards Component b as a part of the serendipitous [CII] detection sample.

Most [CII] systems have only faint tails or slightly extended minor components. Multi-component decomposition will not produce more accurate measurement of LF because, as

we discuss in the sections below, our derived LF is computed in luminosity bin width of 0.5 dex. Small flux boosting due to faint companions will not change our results.

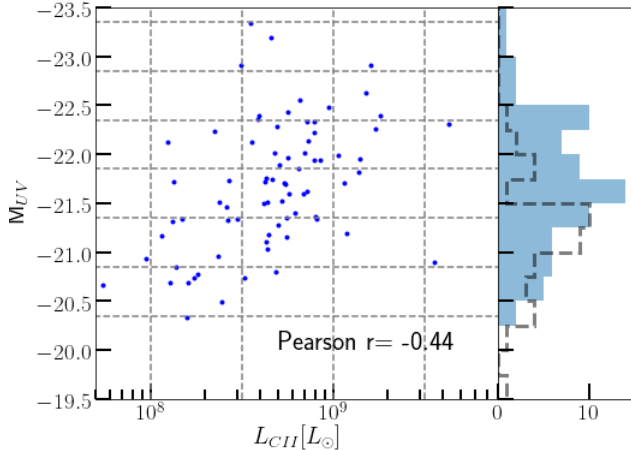


Figure 1. The [CII] luminosities vs observed UV magnitudes for the ALPINE sample. The Pearson r coefficient indicates a weak correlation between these quantities, but with significant scatter. The solid histogram on the right shows the M_{UV} distribution for the sub-sample with [CII] detections, whereas the open dashed histogram shows the same distribution for the [CII] non-detected ALPINE sources.

3. Methodology

3.1. Luminosity function calculation

Our sample is comprised of [CII] observations of UV-selected galaxies. The [CII] sample is a small sub-set of **all** galaxies that meet our UV magnitude cut ($M_{1500A} < -20.2$) from the parent galaxy catalog. Therefore in deriving the luminosity function from our sample, we need to scale the raw number densities from the ALPINE sample to the expected number densities drawn from the known UV luminosity function. This however is not a trivial exercise since as shown in Figure 1 M_{UV} vs. $\log_{10}(L_{[CII]})$ for the ALPINE sample show only a weak correlation with significant scatter.

The most straight forward means of computing the [CII] luminosity function is using a “modified” $1/V_{max}$ method (Schmidt 1968; Felten 1976). We keep the key concept of the maximum and minimum redshifts of a source could have while still being selected by a given survey. The modification to this method is because this is not a blind survey but a targeted survey based on a UV-selected sample. So here we need to account for the incompleteness of our sample relative to the parent sample of UV galaxies. We use C_{UV} to designate the UV completeness correction. For any particular UV magnitude, this correction is the ratio of the expected number of sources as given by the UV luminosity function to the the actual number of ALPINE sources. The calculation of the number density in the i^{th} [CII] luminosity bin is given by Equation 1 below:

$$\phi_i = \frac{1}{\Delta(\log L)} \sum_{j=1}^{N_i} \frac{C(M_{UV,j})}{V_{max,j}} \quad (1)$$

Here, j designates the index of the ALPINE source within the i^{th} [CII] luminosity bin, $C(M_{UV,j})$ gives the UV completeness correction corresponding to the UV magnitude of the j^{th} source and $V_{max,j}$ is the maximum co-moving volume that can be sampled by an ALPINE source with the corresponding [CII] luminosity. Therefore, rather than a naive number density where we sum up all sources within a given luminosity bin and divide by the volume based on our redshift range of interest, we do an effectively weighted sum where the ratio $C_{UV,j}/V_{max,j}$ accounts for the joint probability of having a source of a given UV-magnitude and a given [CII] luminosity within our sample. Below we describe in more detail how this ratio is computed.

As we state above, the C_{UV} correction is defined as the ratio of the expected number of sources at a given UV magnitude to the actual number of sources in the ALPINE sample. We

can write this out as $C(M_{UV}) = \frac{\phi_{UV}\Delta M_{UV}V_{zbin}}{N_{UV,ALPINE}}$. Here ϕ_{UV} is the UV luminosity function. The UV LFs at the ALPINE redshift slices, $z \sim 4.5$ and ~ 5.5 , are computed by interpolations of the $z \sim 4 - 6$ LFs published in [Ono et al. \(2018\)](#), which compiled a catalog of 580,000 galaxies at $z \sim 4 - 7$ over 100 sq.degrees. At $M_{1500\text{\AA}} < -20.2$, this LFs are consistent with previous results by [Finkelstein et al. \(2015\)](#) and [Bouwens et al. \(2015\)](#). The other critical number is $N_{UV,ALPINE}$ which gives us the number of ALPINE sources within the same UV magnitude bins. This is also shown in the right-hand panel of [Figure 1](#). Note that the bin width effectively appears both in the top and bottom of the C_{UV} equation and therefore cancels out. It is only important to have it be not too small in order to have a smooth $N_{UV,ALPINE}$ distribution but also not too large in order to be able to capture the shape of the UV luminosity function. We chose a bin width of $\Delta M_{UV} = 0.5$, but emphasize again that the precise choice is irrelevant as it cancels out. Lastly, to calculate the dimensionless C_{UV} we need to multiply the UV luminosity function by a comoving volume element. This is based on the particular redshift range of interest and therefore is labeled V_{zbin} . The total comoving volume out to redshift z is $V_c(z) = \frac{4\pi}{3}D_M^3(z)$, where the comoving distance $D_M(z) = \frac{c}{H_0} \int_0^z \frac{dz'}{E(z')}$ and $E(z)$ is the dimensionless Hubble parameter which depends on the assumed cosmology. For a particular redshift range and sky coverage, the comoving volume element is simply $\frac{A}{4\pi} \frac{4\pi}{3} [D_M^3(z_{max}) - D_M^3(z_{min})]$ where A is the adopted areal coverage in steradian. For our $V_{max,j}$ in [Equation 1](#), we use the same volume element formulation. The only difference is that we take as the maximum redshift the minimum of the particular source's maximum detectable redshift (given the [CII] detectability limit of ALPINE) or the upper limit

of the redshift range of interest¹. Note that because both $C_{UV,j} \propto A$ and $V_{max,j} \propto A$, [Equation 1](#) implies these A s cancel out and our calculation of ϕ_i does not depend on the adopted A . This arises from the fact that our LF calculation fundamentally scales to the number densities drawn from the UV luminosity function.

[Figure 2](#) shows our calculated C_{UV} for both the lower redshift and higher redshift bins. For the sake of this calculation, we adopted $A = 2$ sq.deg (size of the COSMOS field) but this assumption cancels out in the LF calculation as discussed above. Here C_{UV} was calculated in bins of UV magnitudes of width 0.5, but these values were interpolated so that we can have $C_{UV,j}$ corrections corresponding to each individual source's UV magnitudes in [Equation 1](#). In [Figure 2](#), the error on C_{UV} is derived from the standard deviation of the expected number of galaxies per UV magnitude bin calculated from 1000 Poisson draws per bin. This Poisson uncertainty dominates the uncertainty of the UV LF ([Ono et al. 2018](#)).

The total LF errors are computed as a summation in quadrature of the C_{UV} errors as discussed above and the Poisson error of the $1/V_{max}$ method, which is computed with the following equation (see e.g. [Wyder et al. 2005](#)):

$$\sigma(1/V_{max}) = \frac{1}{\Delta(\log L)} \left[\sum_{j=1}^{N_i} \frac{C_{UV,j}^2}{V_{max,j}^2} \right]^{1/2} \quad (2)$$

Note that this [Equation](#) takes into account the fact that the larger the incompleteness factor C_{UV} , the larger the LF error.

3.2. Accounting for [CII] non-detections

In our method above, we already accounted for the incompleteness of the ALPINE sample

¹ We consider two redshift ranges. The first is $z \sim 4.5$ which covers $z = 4.403 - 4.585$ and the second is $z \sim 5.5$ which covers $z = 5.135 - 5.85$

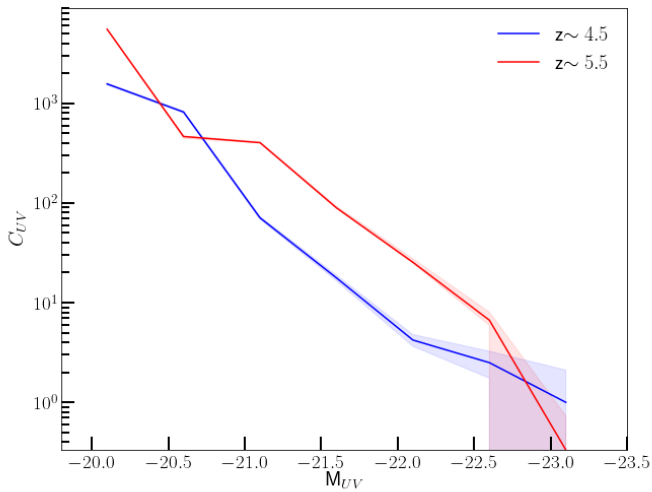


Figure 2. The incompleteness correction C_{UV} as a function of absolute UV magnitude for the two redshift bins. The shaded regions are uncertainties/errors on C_{UV} computed using Monte Carlo simulations as discussed in Section 3.1.

relative to its parent sample of $M_{UV} < -20.2$ sources. However, there is a second type of incompleteness due to [CII] non-detections. Of the 118 ALPINE targets, 43 sources only have [CII] flux limits, with 22 and 21 objects in the $z \sim 4.5$ and the $z \sim 5.5$ (optical spectroscopic redshifts) bin respectively. To account for their maximum potential contribution to the [CII] LFs, we take the non-detections noise estimates, σ , and assign them a maximum luminosity of 3σ . This is a reasonable upper limit for the non-detections, since the distribution of SNR_{peak} for non-detections peaks at ~ 2 (B  thermin et al. 2020) and the threshold for detection is $\text{SNR}_{peak} \sim 3.5$.

Figure 3 shows the contribution of non-detections to our two lowest luminosity bins. We consider three different measurements of the noise, aggressive (lowest noise), normal and secure (highest noise) σ , which are described in Section 3.3 in B  thermin et al. (2020). Figure 3 shows that the distribution of 3σ upper limits measured by the secure method is sys-

tematically shifted to higher luminosity roughly by 0.2 dex compared to that by the aggressive method. We consider the maximum potential contribution of non-detections to each luminosity bin to come from whichever noise estimate maximizes the number of non-detections in the particular bin (i.e. aggressive method at the lower luminosity bin, and the secure method in the higher luminosity bin). Because the non-detections could in principle lie below the 3σ limit, these are the upper limits. We remind the reader that galaxies that are treated with such upper limits lie exclusively in the lowest two luminosity bins so in all other bins, as we discuss below, our estimates are in fact strict lower limits. In forthcoming figures we show both the LFs computed from the detected sources alone, and those that include the maximum potential contribution from the non-detections.

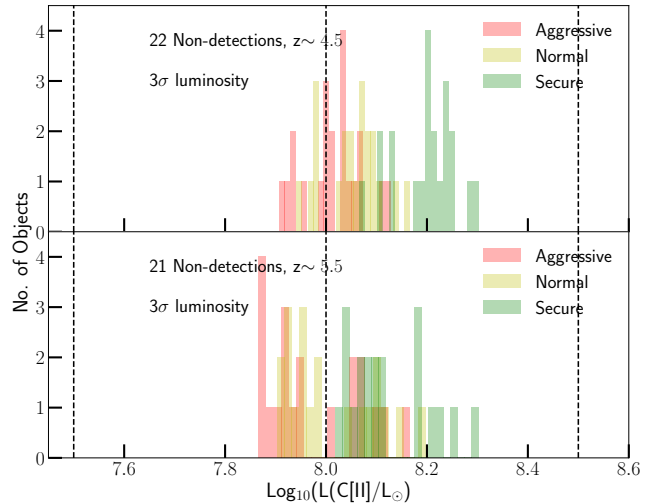


Figure 3. The distributions of 3σ luminosity of non-detected [CII] sources, measured using three different methods. The dashed lines mark the two lowest luminosity bins used for the [CII] LF calculations.

The last type of incompleteness is that ALPINE is not a blind [CII] emission line sur-

vey. Rather it is a survey specifically targeting galaxies selected by 1500Å UV luminosity. The high fraction of [C II] detections in the ALPINE sample implies that the UV selection should detect [C II] emitters efficiently, however the UV luminosity and [C II] line luminosity do not have a tight linear correlation (see Figure 1). The ALPINE selection would certainly miss luminous [C II] emitters with low UV luminosity, *i.e.* $M_{1500\text{Å}} > -20.2$ magnitude. *Thus, the calculated LF based on the UV-selected sample sets the lower bounds to the [C II] LF.* Including our non-detections by assuming they are at 3σ pushes our estimates up, in particular in our two lowest luminosity bins. However, these are still contributions from sources above our UV magnitude limit. To fully account for [C II]-emitters that are potentially UV-faint – *i.e.* below the ALPINE target selection threshold, we need a blind [C II] survey. The ALPINE surveys allows for the next best thing – *i.e.* search for serendipitous sources within the same ALMA data as our targets. This search was conducted by Loiacono et al. (2020). In Section ?? we compare our results with those of Loiacono et al. (2020) who compute the [C II] LFs using serendipitous [C II] sources in the ALPINE survey. Because of potentially uncertain redshift identifications and strong clustering effects, the results from the serendipitous sources should be considered upper bounds. The comparison of the two estimates of the $z \sim 4 - 6$ [C II] luminosity function therefore helps to overcome some of the systematic uncertainties associated with each method and affirm the overall results on the number density and luminosity function of [C II] emitters at these redshifts as seen from the ALPINE survey.

4. Results and discussion

4.1. Measurements based on the ALPINE UV sample

Figure 4 presents our [C II] LFs at $z \sim 4.5$ and $z \sim 5.5$, with the number of sources in each bin labeled. The down-ward arrows mark the upper limits if we include the [C II] non-detections at the two lowest luminosity bins. These are connected by the dashed vertical lines to the points derived using only significant [C II] sources. The errors in Figure 4 include Poisson errors per luminosity bins as well as errors in the incompleteness correction C_{UV} . Table 1 gives our derived LF values at $z \sim 4.5$ and $z \sim 5.5$.

To check the dependence of our results on the specific photometry method, Figure 5 compares the LFs using f_{fit} and $f_{clipped}$. Within the errors, the difference is not significant. In the rest of the analyses, we use the LFs computed from f_{fit} .

From Figure 4, we draw the following conclusions. First, there is no obvious difference between the $z \sim 5$ and $z \sim 0$ LFs at the luminosity range of $\log_{10}(L_{[CII]}/L_{\odot}) \sim 8.25 - 9.25$. But we remind that these LF values are lower limits. Second, we do find some hints of an excess over the $z \sim 0$ LF in the highest luminosity bin $\log_{10}(L_{[CII]}/L_{\odot}) = 9.45 - 9.75$. Lastly, we do not measure significant differences between [C II] LFs at $z \sim 4.5$ and $z \sim 5.5$, within the uncertainties. Considering that LF is essentially the volume density of [C II] emitters, we compute the LF at $z \sim 4-6$ simply by using the geometric mean of the values at $z \sim 4.5$ and $z \sim 5.5$ and the total error as the quadratic sum of individual terms. For simplicity, the subsequent figures show the [C II] LF in a single redshift bin of $4 < z < 6$.

Our key conclusion of the LF excess at high luminosity has large uncertainties. We carry out the following three additional tests to verify this result.

First, as Figure 4 shows, we test using a different binning (open symbols), which gives more sources (4 vs. 2) in the highest luminosity bin

at $z \sim 4.5$. The excess signal is present in both binning methods.

Second, we investigated an alternative means of computing [CII] luminosity function. This method uses the observed M_{UV} vs $L_{[CII]}$ distribution in Figure 1 to construct the probability distribution for sources in each UV magnitude bin for a given $L_{[CII]}$. The expected number density of sources from the UV LF is then spread among the $L_{[CII]}$ bins according to these distributions. Summing the contributions from each UV bin gives us the total number density expected in each $L_{[CII]}$ bin. The results are consistent with our method described above, in that the $z \sim 5$ LF is consistent with $z \sim 0$ LF, except in the highest luminosity bin where we see an excess over the $z \sim 0$ number densities. As in our modified $1/V_{max}$ method, this excess is due to the presence of the [CII]-bright UV-faint outliers clearly seen in Figure 1.

It is worth emphasizing that any UV selected sample such as ALPINE is biased against [CII] emitters with low UV luminosity. Properly counting for these outliers is critical for the [CII] LF calculation.

Third, we examine if blending due to flux boosting could cause the excess signal. We check the [CII] maps (Bethérmin et al. 2020) for the four most luminous sources included in the highest- L bins in Figure 4. Three of the four sources are [CII] bright and single objects, and one has an optical counterpart with very low UV luminosity. The fourth source, deimos_comos_818760, is a triple system and has been published in Jones et al. (2020). The whole system has component C, E and W with $\log_{10}(L_{[CII]}/L_{\odot}) = 9.48, 9.21$ and 8.7 respectively (Jones et al. 2020). With small spatial and velocity separations, component C & E are considered as a major merger (Jones et al. 2020) and is counted as a single source with $\log_{10}(L_{[CII]}/L_{\odot}) = 9.66$ in our calculation. We remind that our LF bin width is 0.5 dex. Com-

ponent W is included in the Loiacono et al. serendipitous sample. The UV counterpart to component C is the ALPINE primary target, however, the counterpart to component E has high dust extinction, and not detected in HST F814W band (Koekemoer et al. 2007, 2011), but detected in deep K -band, with low UV luminosity, M_{1500} well below the ALPINE cutoff. Treating these two components separately will only enhance the key point – that is the existence of a population of bright [CII] emitters with very low UV luminosity. We conclude that blending cannot explain the observed excess at the high end of the luminosity function.

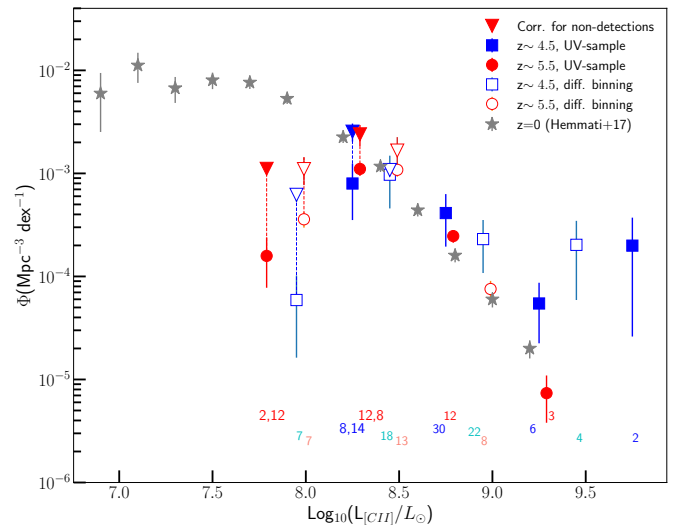


Figure 4. The robust lower bounds on the [CII] emission line luminosity functions at redshift ~ 4.5 (blue squares) and ~ 5.5 (red dots). The open symbols of the same colors use a different binning than the solid points. The gray stars are the [CII] LF at $z \sim 0$ (Hemmati et al. 2017). The downward triangles indicate the upper limits estimated from the [CII] non-detections. The numbers at the bottom indicate the number of sources in the corresponding luminosity bin and redshift. For the comma separated pairs of numbers, the first is the number of [CII] detections, and the second is the number of [CII] non-detections used to compute upper limits. For clarity, we shift the $z \sim 5.5$ data points (red) slightly along the x-axis to avoid overlap.

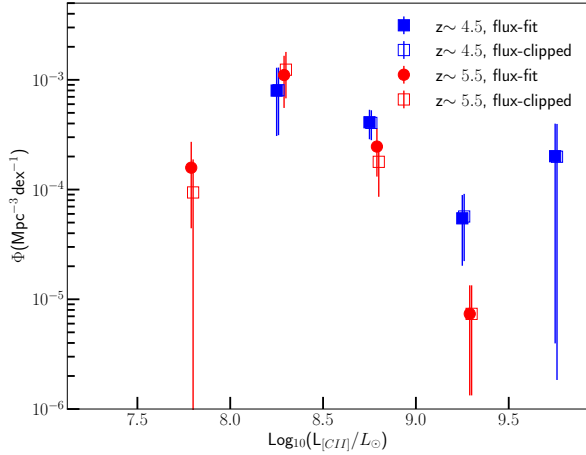


Figure 5. The [CII] LF computed using two different [CII] line fluxes, $f_{clipped}$ and f_{fit}

4.2. Comparison with the [CII] LFs based on serendipitous ALPINE sources

The LFs presented above are lower limits on the number densities of [CII] emitters at $z \sim 4 - 6$ because they miss potential sources that are bright in [CII] but faint in UV. Fortunately, with the 118 ALMA maps along separate pointings, searching for serendipitous [CII] emitters at $4.40 < z < 4.58$ and $5.13 < z < 5.85$ can quantify this effect. In a companion paper, Loiacono et al. (2020) carried out a blind search for all line emitters within the 118 data-cubes. The detailed search algorithm and simulations validating the candidates are presented in Loiacono et al. (2020). We compare our results with that of Loiacono et al. (2020). Their serendipitous sources are split in clustered and field detections, based on their redshift separation from the ALPINE central targets. Figure 6 shows the resulting LFs. The LF based on the serendipitous sources is strongly affected by cosmic clustering and by uncertainties in the identification of some line emitters. Thus it sets an upper boundary to the bright-end of the [CII] luminosity function at $z \sim 4 - 6$, whereas our results are the lower limits. The true [CII] LF

lies somewhere between the purple squares and green dots (shaded area) in Figure 6.

Together, the UV-selected and serendipitous ALPINE samples both point toward significant number densities of luminous [CII] emitters at $z \sim 4 - 6$. At the low luminosity end with $\log_{10}(L_{[CII]}/L_{\odot}) \leq 8.75$ both LFs are consistent with the $z \sim 0$ LF, suggesting no significant evolution in this luminosity range. However, the number densities at $\log_{10}(L_{[CII]}/L_{\odot}) > 9$ are far in excess of the $z \sim 0$ [CII] luminosity function of Hemmati et al. (2017) suggesting potentially considerable evolution.

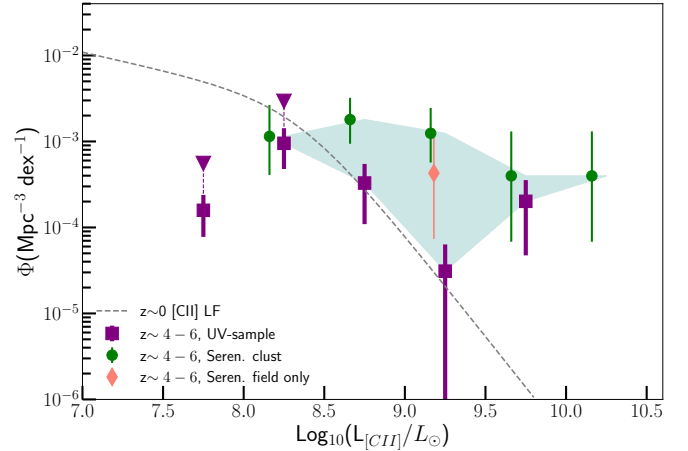


Figure 6. The comparison of [CII] LFs calculated from the UV sample (purple squares) with the estimates from the serendipitous [CII] sources which are in clusters (green) and in field (salmon). These data are taken from Loiacono et al. 2020 and the bins are independent. The dashed line indicates the $z \sim 0$ LF (Hemmati et al. 2017).

4.3. Comparison with indirect observational expectations

In this section, we further test our conclusion above by comparing the direct ALPINE [CII] LFs with indirect estimates of the [CII] luminosity functions based far-IR, and CO luminosity functions at $z \sim 4 - 6$ and adopting typical

conversion relations. Figure 7 shows this comparison. Below we describe in more detail the assumptions behind this figure.

Our first comparison sample is again drawn from serendipitous continuum sources in the ALPINE survey. Here we use the results in Gruppioni et al. (2020) who derive an IR luminosity function based on serendipitously detected *continuum* sources in the ALPINE data. We also use the 250 μm LF from the SCUBA-2 survey (Koprowski et al. 2017). To convert this to a total IR luminosity function, we adopted $L_{\text{IR}}/L_{250\mu\text{m}} = 38.5$ calculated using the infrared spectral energy distribution (SED) template, constructed from data including ALPINE continuum measurements by Béthermin et al. (2020). Finally, to convert both of these into [CII] luminosity functions we adopt the $L_{\text{IR}}/L_{\text{FIR}} = L_{8-1000\mu\text{m}}/L_{42-122\mu\text{m}} = 1.3$ and $\log_{10}(L_{\text{FIR}}/L_{[\text{CII}]}) = 2.69$ recently compiled for high- z galaxies (Zanella et al. 2018).

Next we include the [CII] LFs at $z \sim 5.8$, converted from the CO(1-0) LF published by the ALMA SPECTroscopic Survey (ASPECS, pink shaded region) (Decarli et al. 2019) and from the CO(2-1) LF from the CO Luminosity Density at High Redshift survey (COLDz, light shaded green) (Riechers et al. 2019). Here we use CO(2-1)/CO(1-0) ratio of 1 (Riechers et al. 2019). For comparison, the average value for this ratio is 0.85 for sub-millimeter galaxies. The ASPECS and COLDz CO LFs are published in $L'_{\text{CO}(1-0)}[\text{K km s}^{-1} \text{pc}^2]$. We transformed the CO(1-0) LF to the estimated [CII] LF by using

$$\log_{10}(L_{\text{CO}(1-0)}/L_{\odot}) = \log_{10}(L'_{\text{CO}(1-0)}[\text{K km s}^{-1} \text{pc}^2]) - 4.31 \quad (1)$$

$$\log_{10}[L_{[\text{CII}]} / L_{\text{CO}(1-0)}] = 3.6 \quad (2)$$

Combining Equation (1) and (2), we have $\log_{10}[L'_{\text{CO}(1-0)}/L_{[\text{CII}]}] = 0.9$, which is used to convert the CO(1-0) LF in $L'_{\text{CO}(1-0)}$. The first relation is based on the equations de-

finied in § 2.4 in Carilli & Walter (2013). The $\log_{10}[L_{[\text{CII}]} / L_{\text{CO}(1-0)}]$ ratio can span a range of 3 – 3.8 as measured from a sample of normal galaxies at $z \sim 0$ and $z \sim 1 - 2$ (Stacey et al. 1991, 2010). Zanella et al. (2018) recently examined a larger sample of galaxies with published $L_{[\text{CII}]}$ and L_{CO} measurements at $z \sim 0 - 6$. We adopt the value of 3.6 in Equation (2), consistent with the calculation of molecular mass described in § 4.5. Our adopted value makes a conservative conversion to [CII] luminosity. Extremely metal-poor, low mass, blue compact dwarf galaxies can have one order of magnitude higher [CII]-to-CO(1-0) ratio (Cormier et al. 2014). But these are unlikely to be good analogues, since the averaged star formation efficiency for the ALPINE sample is an order of magnitude higher than the local sample (Faisst et al. 2019; Madden et al. 2013; Cormier et al. 2014). In addition, our adopted value ignores that at $z \sim 4 - 6$, CMB photons will increase line excitation as well as background for CO(1-0) line (da Cunha et al. 2013). The CO(1-0) line would be suppressed by $\sim 20\%$ at $z \sim 6$ (Vallini et al. 2018). This would potentially push these estimated [CII] LFs to even higher luminosities, but is still well within the overall uncertainties in this conversion relation.

Figure 7 shows that within the large uncertainties, there is good agreement between all these constraints on the [CII] luminosity function at $z \sim 4 - 6$. Combined, they strengthen even further our conclusion that there has been strong evolution in the number densities of $L_{[\text{CII}]} > 10^9 L_{\odot}$ sources between $z \sim 5$ and $z \sim 0$.

Finally, including the data from our work, Loiacono et al. (2020), the converted values using the FIR LFs from Gruppioni et al. (2020) and (Koprowski et al. 2017), we perform a fit to the data assuming a Schechter function. We derive $\log_{10}(L_{[\text{CII}]}^*/L_{\odot}) = 9.5 \pm 0.6$, $\phi^* = (8.4 \pm$

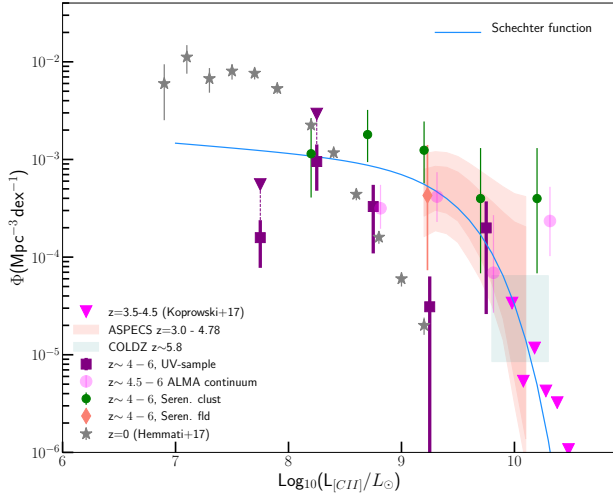


Figure 7. The [CII] emission line luminosity functions derived from the UV sample (purple symbols) and the serendipitous, confirmed [CII] emitters at $z \sim 4 - 6$ (green circles and red diamond). Also included are the [CII] LFs converted from the ALPINE IR LF (light pink circles) (Gruppioni et al. 2020), from the SCUBA-2 rest-frame $250\mu\text{m}$ LF at $z \sim 3.5 - 4.5$ (dark pink triangles) (Koprowski et al. 2017), and from the CO LF published by ASPECS (Decarli et al. 2019) and COLDz (Riechers et al. 2019). The pink shade region represents both 1σ and 2σ uncertainty regions from Decarli et al. (2019). The blue solid line is the Schechter functional form fit to all of the data, including the estimated [CII] LF values based on FIR LFs

$8) \times 10^{-4} \text{Mpc}^{-3} \text{dex}^{-1}$ and $\alpha = -1.1 \pm 0.3$ ². Because our results and the Loiacono et al. (2020) are only the lower and upper bounds, and the converted LF from FIR are affected by large systematic uncertainties, large errors are expected. Presenting them here is for the convenience when making comparison of the total [CII] emission line luminosity density. At face value, the $z \sim 4 - 6$ $L_{[\text{CII}]}$ has increased by a

² The fit was done using the CURVE_FIT function within the SCIPY package (Jones et al. 2001–).

factor of 20 compared to $L_{[\text{CII}]}^* \sim 2.2 \times 10^8 L_{\odot}$ at $z \sim 0$ (Hemmati et al. 2017).

4.4. Comparison with theoretical predictions

Figure 8 shows the model [CII] LFs from Popping et al. (2016) and Lagache et al. (2018) overlaid on the same data as shown in Figure 7. These models combine semi-analytic galaxy evolution models with radiative transfer calculations to make predictions on [CII] line emissions and LFs. As already noted in our $z \sim 0$ [CII] LF paper (Hemmati et al. 2017), the Popping et al. (2016) model is definitely ruled out by the observations. Lagache et al. (2018) model is much improved, but still fails to match the abundant luminous [CII] emitters at $z \sim 4 - 6$. The Lagache et al. (2018) model is reasonably consistent with the data at $\log_{10}(L_{[\text{CII}]} / L_{\odot}) > 10$, but the data overall are more consistent with a Schechter functional form than the power law form of this model.

Several cosmological simulations have investigated CO(1-0) and [CII] emission at high- z , most of them focusing on the $L([\text{CII}])$ -SFR relation and associated deviations. As illustrated in Ferrara et al. (2019), the physical processes of [CII] emission are complex, and the assumed gas density in PDRs (or size and filling factor), ionization factor, metallicity and starburstness can all affect [CII] luminosity. Some models can reproduce both the luminous and weak [CII] sources in the $L([\text{CII}])$ -SFR plane (Vallini et al. 2015; Lagache et al. 2018; Ferrara et al. 2019). The discrepancy between our LF and the models however implies that the current models for synthesizing the high- z [CII] populations likely involves other factors that are still not well understood. More work is clearly needed.

4.5. Implications to the molecular gas mass density at $z \sim 4 - 6$

It has been widely recognized that the evolution of the molecular gas mass as a function of redshift holds clues to understanding galaxy

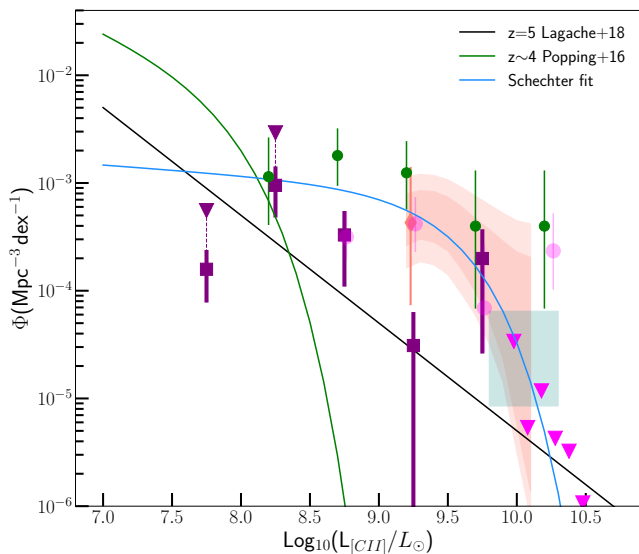


Figure 8. The comparison of the [CII] LF measurements from both the UV (purple) and [CII] serendipitous samples (green and pink dots) with the model predictions (black and green lines). Here we also included the [CII] LFs converted from the FIR and CO LFs. See text for the details. For additional figure legend see Figure 7 for the data points.

formation and evolution more broadly (for a review see Carilli & Walter 2013). In particular, we want to compare with the model for ρ_{molgas} as a function of z from Liu et al. (2019). Liu et al. (2019) combined their ALMA galaxy catalog with 20 other published datasets and made a comprehensive analysis of scaling relations between stellar mass, gas fraction and redshift. They expressed the molecular gas mass density, $\rho_{mol}(z) = \sum_{M_*} \Phi_{SMF}(z, M_*) \times M_* \times \mu_{gas}(z, M_*, \Delta MS)$, as a function of stellar mass function Φ and gas fraction μ . They integrate down to $M_* = 10^9 M_\odot$. Using the Liu et al. (2019) $\mu_{molgas} = M_{molgas}/M_* \sim 2$ at $z \sim 5$ and $\alpha_{[CII]-M_{molgas}} \sim 30 M_\odot/L_\odot$ from Zanella et al. (2018), this lower limit translates to $L_{[CII]} \sim 7 \times 10^7 L_\odot$. Therefore we start by integrating the [CII] luminosity function down

to this limit giving us a luminosity density of $\mathcal{L}_{[CII]}$ is $1.2 \times 10^6 L_\odot \text{Mpc}^{-3}$. Zanella et al. (2018) find that $\alpha_{[CII]-M_{molgas}}$ relation has an 1σ of 0.3 dex, translating into a linear ratio $M_{mol}/L_{[CII]} = 15 - 60 M_\odot/L_\odot$. We calculate the cosmic volume averaged molecular mass density $\rho_{molgas} = (2 - 7) \times 10^7 M_\odot/\text{Mpc}^3$ at $z \sim 4 - 6$. At 2σ and 95% confidence level, we estimate $\rho_{molgas} = (1 - 14) \times 10^7 M_\odot/\text{Mpc}^3$.

Note however, that when using the Zanella et al. (2018) relation on individual ALPINE galaxies to convert their $L_{[CII]}$ into the molecular gas mass, we see that the mean gas fraction is $\mu_{molgas} \approx 3$ (Dessauges-Zavadsky et al. 2020). This is slightly higher than in the one of the Liu et al. (2019) sample likely due to the fact that the ALPINE galaxies have lower stellar masses than the Liu et al. (2019) sample. We checked that changing this constant does not change our results in any substantive way (see the discussion below).

In Figure 9, we overlay our estimates of ρ_{molgas} on the Liu et al. (2019) model predictions (based on the A3COSMOS sample). We also overlay the 1 and 2σ constraints from ASPECS (Decarli et al. 2019) and COLDz (Riechers et al. 2019) which surveys measured CO transitions using ALMA and JVLA and set constraints on the mass density of molecular gas at $z \sim 3 - 6$. This cross-check is critical because all these surveys have pros and cons in their attempts to constrain the evolution of the cosmic molecular gas density. The key advantage of the ALPINE survey is its large sample (thanks to the [CII] line being a significantly brighter tracer of molecular gas than any CO line), but due to the uncertainties in the selection function we are left with only lower and upper bounds on the LF. The A3COSMOS-based constraint is also affected by selection biases. Both ASPECS and COLDz, while smaller samples, have the key advantage of being unbiased in terms of cold gas selection, since they use CO which is the most

reliable tracer of cold molecular gas mass currently known. Figure 9 shows that, within the uncertainties, all these studies are consistent. As such, these surveys provide supporting evidence that we are obtaining useful constraints as we use the sizeable ALPINE sample to constrain the cold gas density vs redshift relation.

Figure 9 shows that our results are well within the range of the Liu et al. (2019) model, only slightly favoring the upper half. The spread in the model shown indicates different assumption of the molecular gas fraction as a function of redshift. The upper limit is based on Scoville et al. (2017) analyses of the ALMA dust continuum observations at $z < 3.8$, and the lower limit is based on the Tacconi et al. (2018) relation, primarily from the PHIBBS CO survey at $z < 2.5$. In contrast to our results, the results of the CO surveys (COLDz and ASPECS) favor the lower half of the models shown. However, given the large uncertainties in all of these estimates, this slight tension between us and the CO survey is not too significant. Within the 2σ uncertainties, our results are consistent with those from COLDz and ASPECS.

Dessauges-Zavadsky et al. (2020) also examined the molecular gas content of individual ALPINE galaxies at $z \sim 5$, using [C II] detections to constrain the total molecular gas mass at $z \sim 5$. Like us, they use the scaling relations from Zanella et al. (2018). They find $\mu_{molgas} \approx 3$ which leads to slightly lower total mass density and a better agreement with the Tacconi et al. (2018) model (see Fig. 7 of their paper). Indeed, given the large uncertainties on these molecular gas mass densities, we cannot really exclude any of the models. The main difference between our analyses however is that our calculation is based on our best estimate of the [C II] luminosity function, including all three ALPINE constraints thereof (the UV-sample, the serendipitous sample and the continuum-sample) as well as the far-IR LF from Koprowski

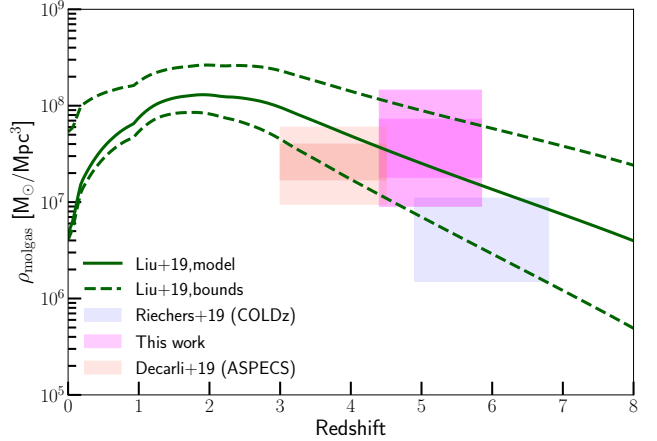


Figure 9. The estimated mass density of molecular gas based on our [C II] LF (pink shaded region). The height of this pink region corresponds to 2σ and 1σ of the M_{mol} - $L_{[CII]}$ scaling constant. Similarly, the ASPECS result (salmon shaded region) also includes 2σ and 1σ uncertainties.

et al. (2017). In this paper we do not look at the ALPINE constraints on the star-formation rate density at $z \sim 5$. This question is examined in our companion paper, Loiacono et al. (2020).

5. Summary and conclusions

The ALPINE survey carried out ALMA band-7 observations of 118 galaxies at $z \sim 4.40 - 5.85$ selected by their UV luminosity ($M_{1500\text{\AA}} < -20.2$, or $L_{1500\text{\AA}} > 0.6L_{1500\text{\AA}}^*$) within the COSMOS and GOODS-South fields. The observations show a high fraction (75/118) of [C II] detections confirming that, at high- z , [C II] line emission broadly traces the UV emission, especially for galaxies without substantial dust obscuration.

Using the ALPINE UV selected target sample, we calculate the lower bounds to the true volume densities of [C II] emitters as a function of line luminosity. Based on the UV selected sample alone, we see a hint of excess in [C II] LF at $\log_{10}(L_{[CII]}/L_{\odot}) \geq 9.5$. We compare our results with the [C II] LFs derived from the serendipitous [C II] sample of Loiacono et al. (2020) which provide the upper bounds. Taken together, the two different LF estimates from

the ALPINE data, show potentially considerable redshift evolution in the bright end of the [CII] LF at $z \sim 4 - 6$ compared to $z \sim 0$. We fit a single Schechter function model to both these ALPINE constraints as well indirect [CII] LFs converted from published far-IR and CO(1-0) LFs at $z \sim 4 - 5$. This model fit suggests that the population of luminous [CII] emitters at $z \sim 4 - 6$ is roughly $20 - 50 \times$ more abundant than that of the local Universe.

By integrating the [CII] LF, and adopting scaling relations between [CII] uminosity and molecular gas mass we estimate that the molecular mass density at $z \sim 4 - 6$ reaches roughly $(2 - 7) \times 10^7 M_{\odot} \text{Mpc}^{-3}$ (1σ). This value is consistent with the evolutionary tracks of $\rho_{mol}(z)$ from Liu et al. (2019), favoring slightly models with somewhat higher galaxy gas fractions. By contrast, CO surveys such as COLDz and ASPECS Riechers et al. (2019); Decarli et al. (2019) favor slightly lower gas fractions. However, this difference is not significant at present given the large uncertainties in all the measurements.

Our measurements at $z \sim 4 - 6$ have important implications for upcoming millimeter spectral surveys such as CONCERTO (Lagache 2018b) and CCAT-Prime (Stacey et al. 2018). They provide benchmarks of the expected number of sources, in particular predicting that large area millimeter spectral surveys should find many extremely luminous [CII] emitters at $z \sim 4 - 6$.

Finally, our results are in tension with the available model predicted LFs, particularly at the luminous end (Popping et al. 2016; Lagache et al. 2018) suggesting model assumptions about the physical conditions in PDR at these redshifts may not be correct. Better understanding of the physical conditions in the ISM at

these redshifts is clearly needed. This would be enabled by a far-IR spectroscopy survey facility such as the proposed Origins Space Telescope³.

We thank Liu, Daizhong from Max-Planck-Institut für Astronomie for sending us their results in electronic form. This paper is based on data obtained with the ALMA Observatory, under Large Program 2017.1.00428.L. ALMA is a partnership of ESO (representing its member states), NSF(USA) and NINS (Japan), together with NRC (Canada), MOST and ASIAA (Taiwan), and KASI (Republic of Korea), in cooperation with the Republic of Chile. The Joint ALMA Observatory is operated by ESO, AUI/NRAO and NAOJ. GL acknowledges support from the European Research Council (ERC) under the European Unions Horizon 2020 research and innovation programme (project CONCERTO, grant agreement No 788212) and from the Excellence Initiative of Aix-Marseille University-A*Midex, a French Investissements dAvenir programme. AC, CG, FL, FP and MT acknowledge the support from grant PRIN MIUR 2017 - 20173ML3WW_001. ST acknowledge support from the European Research Council (ERC) Consolidator Grant funding scheme (project ConTExt, grant number: 648179). The Cosmic Dawn Center (DAWN) is funded by the Danish National Research Foundation under grant No. 140. Our research made use of Astropy,⁴ a community-developed core Python package for Astronomy (Astropy Collaboration et al. 2013; Price-Whelan et al. 2018). LV acknowledges funding from the European Unions Horizon 2020 research and innovation program under the Marie Skłodowska-Curie Grant agreement No. 746119. G.C.J. acknowledges ERC Advanced Grant 695671 “QUENCH” and support by the Science and Technology Facilities Council (STFC).

³ <https://asd.gsfc.nasa.gov/firs/>

⁴ <http://www.astropy.org>

References

- Astropy Collaboration, Robitaille, T. P., Tollerud, E. J., et al. 2013, *A&A*, **558**, A33
- Barro, G., Kriek, M., Pérez-González, P. G., et al. 2017, *ApJL*, **851**, L40
- Bethermin, M., Fudamoto, Y., Ginolfi, M., et al. 2020, *arXiv*, [arXiv:2002.00962](https://arxiv.org/abs/2002.00962)
- Bouwens, R. J., Illingworth, G. D., Oesch, P. A., et al. 2015, *ApJ*, **803**, 34
- Capak, P. L., Carilli, C., Jones, G., et al. 2015, *Nature*, **522**, 455
- Carilli, C. L., & Walter, F. 2013, *ARA&A*, **51**, 105
- Carniani, S., Maiolino, R., Amorin, R., et al. 2018, *MNRAS*, **478**, 1170
- Cormier, D., Madden, S. C., Lebouteiller, V., et al. 2014, *A&A*, **564**, A121
- da Cunha, E., Groves, B., Walter, F., et al. 2013, *ApJ*, **766**, 13
- Decarli, R., Walter, F., González-López, J., et al. 2019, *ApJ*, **882**, 138
- Dessauges-Zavadsky, M., Ginolfi, M., Pozzi, F., et al. 2020, *arXiv*, [arXiv:2004.10771](https://arxiv.org/abs/2004.10771)
- Emonts, B. H. C., De Breuck, C., Lehnert, M. D., et al. 2015, *A&A*, **584**, A99
- Faisst, A., Bethermin, M., Capak, P., et al. 2019, *arXiv*, [arXiv:1901.01268](https://arxiv.org/abs/1901.01268)
- Faisst, A. L., Schaerer, D., Lemaux, B. C., et al. 2020, *ApJS*, **247**, 61
- Felten, J. E. 1976, *ApJ*, **207**, 700
- Ferrara, A., Vallini, L., Pallottini, A., et al. 2019, *MNRAS*, **489**, 1
- Finkelstein, S. L., Ryan, Russell E., J., Papovich, C., et al. 2015, *ApJ*, **810**, 71
- Freundlich, J., Combes, F., Tacconi, L. J., et al. 2019, *A&A*, **622**, A105
- Fudamoto, Y., Ivison, R. J., Oteo, I., et al. 2017, *MNRAS*, **472**, 2028
- Goldsmith, P. F., Langer, W. D., Pineda, J. L., & Velusamy, T. 2012, *ApJS*, **203**, 13
- Hemmati, S., Yan, L., Diaz-Santos, T., et al. 2017, *ApJ*, **834**, 36
- Jones, E., Oliphant, T., Peterson, P., et al. 2001–, SciPy: Open source scientific tools for Python
- Jones, G. C., Carilli, C. L., Shao, Y., et al. 2017, *ApJ*, **850**, 180
- Jones, G. C., Bethermin, M., Fudamoto, Y., et al. 2019, *arXiv*, [arXiv:1908.07777](https://arxiv.org/abs/1908.07777)
- Jones, G. C., Béthermin, M., Fudamoto, Y., et al. 2020, *MNRAS*, **491**, L18
- Katz, H., Kimm, T., Sijacki, D., & Haehnelt, M. G. 2017, *MNRAS*, **468**, 4831
- Koekemoer, A. M., Aussel, H., Calzetti, D., et al. 2007, *ApJS*, **172**, 196
- Koekemoer, A. M., Faber, S. M., Ferguson, H. C., et al. 2011, *ApJS*, **197**, 36
- Koprowski, M. P., Dunlop, J. S., Michałowski, M. J., et al. 2017, *MNRAS*, **471**, 4155
- Lagache, G. 2018b, *IAU Symposium*, **333**, 228
- Lagache, G., Cousin, M., & Chatzikos, M. 2018, *A&A*, **609**, A130
- Le Fèvre, O., Béthermin, M., Faisst, A., et al. 2019, *arXiv*, [arXiv:1910.09517](https://arxiv.org/abs/1910.09517)
- Lelli, F., De Breuck, C., Falkendal, T., et al. 2018, *MNRAS*, **479**, 5440
- Liu, D., Schinnerer, E., Groves, B., et al. 2019, *ApJ*, **887**, 235
- Madden, S. C., Rémy-Ruyer, A., Galametz, M., et al. 2013, *PASP*, **125**, 600
- Olsen, K., Greve, T. R., Narayanan, D., et al. 2017, *ApJ*, **846**, 105
- Ono, Y., Ouchi, M., Harikane, Y., et al. 2018, *PASJ*, **70**, S10
- Pallottini, A., Ferrara, A., Decataldo, D., et al. 2019, *MNRAS*, **487**, 1689
- Popping, G., van Kampen, E., Decarli, R., et al. 2016, *MNRAS*, **461**, 93
- Price-Whelan, A. M., Sipőcz, B. M., Günther, H. M., et al. 2018, *AJ*, **156**, 123
- Riechers, D. A., Carilli, C. L., Capak, P. L., et al. 2014, *ApJ*, **796**, 84
- Riechers, D. A., Pavesi, R., Sharon, C. E., et al. 2019, *ApJ*, **872**, 7
- Schmidt, M. 1968, *ApJ*, **151**, 393
- Scoville, N., Lee, N., Vanden Bout, P., et al. 2017, *ApJ*, **837**, 150
- Shao, Y., Wang, R., Jones, G. C., et al. 2017, *ApJ*, **845**, 138
- Stacey, G. J., Geis, N., Genzel, R., et al. 1991, *ApJ*, **373**, 423
- Stacey, G. J., Hailey-Dunsheath, S., Ferkinhoff, C., et al. 2010, *ApJ*, **724**, 957
- Stacey, G. J., Aravena, M., Basu, K., et al. 2018, *Proc. SPIE*, **10700**, 107001M
- Tacconi, L. J., Genzel, R., Saintonge, A., et al. 2018, *ApJ*, **853**, 179
- Vallini, L., Gallerani, S., Ferrara, A., et al. 2015, *ApJ*, **813**, 36
- Vallini, L., Pallottini, A., Ferrara, A., et al. 2018, *MNRAS*, **473**, 271
- Wang, R., Wagg, J., Carilli, C. L., et al. 2013, *ApJ*, **773**, 44
- Willott, C. J., Carilli, C. L., Wagg, J., & Wang, R. 2015, *ApJ*, **807**, 180
- Wyder, T. K., Treyer, M. A., Milliard, B., et al. 2005, *ApJL*, **619**, L15
- Zanella, A., Daddi, E., Magdis, G., et al. 2018, *MNRAS*, **481**, 1976

Table 1. ALPINE [CII] LFs at $z \sim 4 - 6$ in $10^{-4} \text{ Mpc}^{-3} \text{ dex}^{-1}$

$\text{Log}_{10}(L_{[\text{CII}]})$	ϕ_{UV}^a	$\phi_{UV}^{up,b}$	ϕ_{UV}	$\phi_{UV}^{up,c}$
L_{\odot}	$z \sim 4.5$		$z \sim 5.5$	
7.75	1.58 ± 0.81	...
8.25	7.98 ± 4.45	25.4 ± 3.5	11.1 ± 1.6	24.0 ± 5.5
8.75	4.12 ± 2.18	...	2.47 ± 0.35	...
9.25	0.55 ± 0.32	...	0.074 ± 0.036	...
9.75	2.0 ± 1.73

NOTE—**a**: ϕ_{UV} is the [CII] LF derived based on the ALPINE primary targets, *i.e.* the UV sample. **b & c**: ϕ_{UV}^{up} refers to the corrected [CII] LFs by taking into account of the [CII] non-detections in the ALPINE sample. These mark the upper limits to the two lower luminosity bins because we assume that these non-detections have 3σ line luminosity.